
Automated Detection of Breast Mass Spiculation Levels and Evaluation of Scheme Performance¹

Luan Jiang, MSc, Enmin Song, PhD, Xiangyang Xu, MSc, Guangzhi Ma, MSc, Bin Zheng, PhD

Rationale and Objectives. Although the spiculation levels of breast mass boundaries are a primary sign of malignancy for masses detected on mammography, developing an automated computerized method to detect spiculation levels and quantitatively evaluating the performance of such a method is a difficult task. The objectives of this study were to (1) develop and test a new method to improve mass segmentation and detect mass boundary spiculation levels and (2) assess the performance of this method using a relatively large imaging data set.

Materials and Methods. The fully automated method developed for this study includes three image-processing steps. In the first step, the principle of maximum entropy is applied in the selected region of interest (ROI) after correcting the background trend to enhance the initial outlines of a mass. In the second step, an active-contour model is used to refine the initial outlines. In the third step, spiculated lines connected to the mass boundary are detected and identified using a special line detector. A quantitative spiculation index is computed to assess the degree of spiculation. To develop and evaluate this automated method, 211 ROIs depicting masses were extracted from a publicly available image database. Among these ROIs, 106 depicted circumscribed mass regions and 105 involved spiculated mass regions. The performance of the method was evaluated using receiver-operating characteristic (ROC) analysis.

Results. The computed area under the ROC curve, when applying the method to the data set, was 0.701 ± 0.027 . By setting up a threshold at a spiculation index of 5.0, the method achieved an overall classification accuracy of 66.4%, with 54.3% sensitivity and 78.3% specificity.

Conclusions. In this study, a new computerized method with a number of unique characteristics was developed to detect spiculated mass regions, and a simple spiculation index was applied to quantify mass spiculation levels. Although this quantitative index can be used to distinguish between spiculated and circumscribed masses, the results also suggest that the automated detection of mass spiculation levels remains a technical challenge.

Key Words. Computer-aided diagnosis; mammography; mass segmentation; mass spiculation.

© AUR, 2008

Breast cancer is among the leading causes of death in women (1,2). The early detection and treatment of breast cancer can substantially reduce patient mortality and morbidity (3). For the early detection of breast cancer, mammography is widely used and is among the most reliable and cost-effective methods (4,5). However, in the clinical environment, reading mammograms is a time-consuming and low-specificity task for most radiologists. To help improve radiologists' reading efficiency and interpretation performance, a large number of computer-aided detection or computer-aided diagnosis (CAD) methods have been developed and tested (6). Currently, commercialized CAD

Acad Radiol 2008; 15:1534–1544

¹ From the Center for Biomedical Imaging and Bioinformatics, School of Computer Science and Technology, Huazhong University of Science and Technology, Wuhan 430074, China (L.J., E.S., X.X., G.M.); and the Department of Radiology, University of Pittsburgh, Pittsburgh, PA (B.Z.). Received June 2, 2008; accepted July 11, 2008. This study was supported in part by grant 2006AA02Z347 from the National 863 High Technology Research and Development Program of China and grant R01-101733 from the National Cancer Institute, Bethesda, MD, to the University of Pittsburgh. **Address correspondence to:** E.S. e-mail: esong@mail.hust.edu.cn

© AUR, 2008

doi:10.1016/j.acra.2008.07.015

methods have achieved very high performance in detecting microcalcification clusters (eg, 98% sensitivity with 0.2 false-positive clusters per image [7]), although their performance in mass detection remains relatively low (8). As a result, using CAD has substantially improved radiologists' performance and efficiency in detecting microcalcification clusters (9). However, because of radiologists' low confidence in CAD-cued masses, most CAD-cued false-negative masses are discarded as false-positive detections in the screening environment (10).

A large number of studies have been conducted in an attempt to improve the performance of CAD in mass detection (6). One approach focuses on improving mass segmentation accuracy and identifying effective image features. Previous studies have suggested that improving the accuracy of mass region segmentation could also significantly improve the performance of CAD in mass detection and characterization (11,12). The segmentation of masses on original images is often difficult when the masses overlap with surrounding dense-tissue parenchyma. Several automated and semi-automated methods focusing on this problem have been developed (13–17). These include using a density-weighted contrast enhancement algorithm that combines adaptive filtering and edge detection (13), an adaptive multilayer topographic regional growth algorithm (14), a gray-level-based iterative and linear segmentation algorithm (15), a dynamic programming approach (16), and dynamic contour modeling (17) to segment mass lesions from surrounding breast tissue.

One important feature in automated mass detection and classification is mass boundary spiculation level (18). A number of previous studies have been conducted in an attempt to automatically detect spiculated masses and incorporate this feature into CAD methods (19–22). Kegelmeier et al (19) detected spiculated masses using local edge orientation and Laws texture features. In their algorithm, a statistical classifier is applied to labeling each pixel with its probability of being located on an abnormality, but it is not applicable for the detection of non-spiculated masses. Karssemeijer and Te Brake (20) used a method based on the statistical analysis of a map of pixel orientations to detect stellate distortions on mammograms. Huo et al (21) developed a new spiculation-sensitive pattern recognition technique to quantify the degree of spiculation of a lesion and classified masses as malignant or benign. They reported that the computer-extracted spiculation measure was shown to yield higher classification accuracy than the spiculation rating of an experienced radiologist. Sahiner et al (22) presented a fully automated

and three-stage segmentation method that included clustering, active contour, and spiculation detection stages to detect spiculated and nonspiculated masses. The results indicated that combining texture features with morphologic features extracted from automatically segmented mass regions was an effective approach for the automated characterization of mammographic masses. Recent studies of interactive CAD methods have also suggested that the accurate detection and classification of mass boundary spiculation levels plays an important role in improving the visual similarity of similar reference mass regions selected by interactive CAD methods (23).

Although significant research effort has gone into developing computerized methods to detect mass boundary spiculation levels, the accurate and robust detection of mass spiculation remains a technical challenge because the spiculated patterns are often subtle and varied in appearance, and image subsampling is frequently used in mass detection methods (12). In addition, because of the lack of "ground truth" of mass spiculation levels in the testing data set, assessing the performance of a method is also difficult.

In this study, we developed and tested a new computerized method whose aim is to obtain an accurate delineation of mass boundaries and quantification of boundary spiculation levels. This fully automated method includes three main steps. In the first step, the principle of maximum entropy is used to detect the initial mass outlines (boundary contours) in the region of interest (ROI) after correcting for noisy background trend. In the second step, an active-contour model is applied to refine the initially detected mass boundary contours. In the third step, a line detector is used to detect and identify spiculated lines connected to the mass boundary. On the basis of the final region segmentation, a quantitative measure (feature), the spiculation index (SI), is used to assess the degree of spiculation. The performance of the method using the SI for classifying identified mass regions was evaluated using a relatively large image data set and the area under the receiver-operating characteristic (ROC) curve.

MATERIALS AND METHODS

Selection of Image Data Set

The images used in this study were selected from a publicly available database, the Digital Database for Screening Mammography (DDSM), assembled by a research group at the University of South Florida (24). This database has been selected and used in developing a num-

Table 1
Detailed Description of the Selected Image Data Set

Digitizer	Circumscribed Masses	Spiculated Masses
Lumisys	70	44
Howtek	36	61
Total	106	105

ber of CAD methods (15,25). The criteria for the inclusion of an image in the data set for this study were that the image contained circumscribed and irregular spiculated masses subjectively classified by radiologists and recorded in the DDSM. We selected both malignant and benign masses that met the inclusion criteria of this study.

For image selection, we first used software provided by the Michael Heath Computer Vision Laboratory at the University of South Florida (24) to uncompress the images. Then the raw data of images that were digitized using both Lumisys (Marietta, GA) and Howtek (Aztek, Inc., Irvine, CA) digitizers were subsampled using an average of 8×8 pixel values (ie, increasing the pixel size from 50×50 to $400 \times 400 \mu\text{m}$ when using the Lumisys digitizer). We also compressed the range of image pixel gray level from 12 to 8 bits. In the DDSM, each image depicting abnormal masses has a corresponding overlay file that records detailed information about each mass region, including lesion type, the Breast Imaging Reporting and Data System assessment, the pathologic classification (malignant or benign), a subjective rating of lesion subtlety, and a visual assessment of boundary margin characteristics. Mass boundaries in the DDSM have been subjectively characterized as (1) spiculated, (2) circumscribed, (3) ill defined, (4) microlobulated, and (5) obscured. In this study, we selected only ROIs that depicted spiculated or circumscribed masses. To regularly extract each ROI, we first manually marked a point (pixel) near the subjectively estimated geometric center of the mass. After applying a window of 15×15 pixels centered at the marked pixel, our computerized method searched for a pixel with the minimum gray level (digital value) inside the window. Then, using this pixel as the center, the method automatically extracted the ROI that covered the selected mass region. Each extracted ROI included 128×128 pixels (ie, $51.2 \times 51.2 \text{ mm}$ for images digitized using the Lumisys digitizer).

The selected test data set consisted of 106 ROIs involving circumscribed mass regions and 105 ROIs involving spiculated mass regions from 206 mammograms of

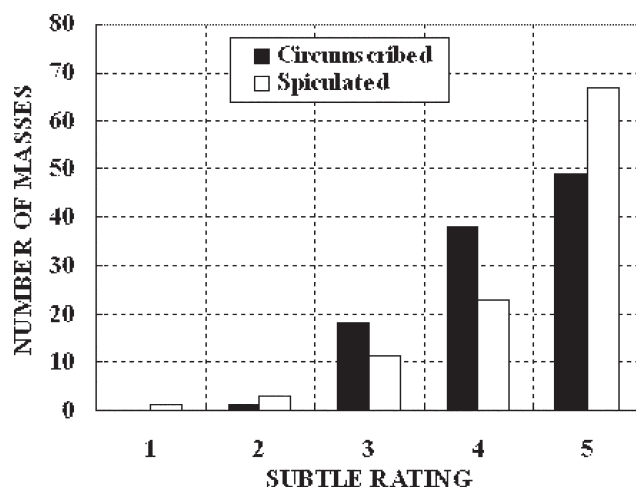


Figure 1. Distribution of the subtlety ratings of the regions of interest in our data set, as given in the Digital Database for Screening Mammography.

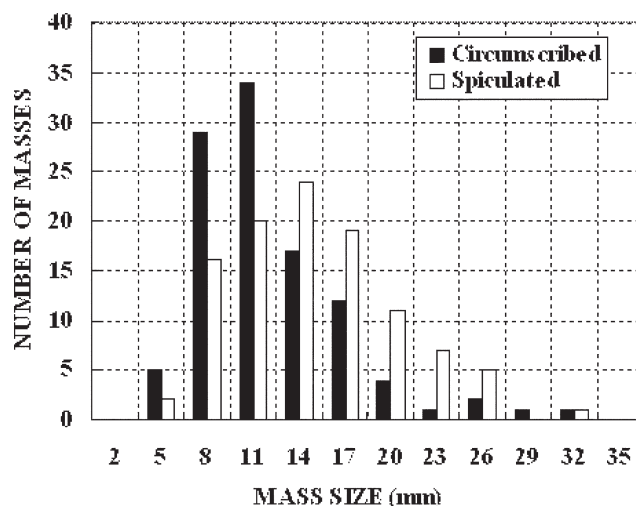


Figure 2. Distribution of the mass sizes of the regions of interest in our data set.

144 patients (Table 1). The subtlety of each abnormality recorded in the DDSM ranges from 1 (subtle) to 5 (obvious). A histogram of the subtlety ratings of the selected ROIs is plotted in Figure 1. The distribution of the sizes of the selected mass regions is shown in Figure 2, indicating that the distribution of the sizes for both circumscribed and spiculated masses was similar. The mean sizes of the circumscribed masses and the spiculated masses were 12.2 and 14.8 mm, respectively, in the selected data set. Table 2 summarizes the density assessment distribution of normal breast tissue surrounding each identified mass using Breast Imaging Reporting and Data System ratings for all cases in the data set.

Table 2
Distribution of BI-RADS Assessments of Breast Tissue
Composition for All Selected Cases in the Data Set

	BI-RADS Rating*			
	1	2	3	4
Mass	1	2	3	4
Circumscribed	13	37	18	4
Spiculated	8	32	19	13
Total	21	69	37	17

BI-RADS, Breast Imaging Reporting and Data System.

*Rating categories 1 to 4 represent "almost entirely fat," "scattered fibroglandular densities," "heterogeneously dense," and "extremely dense."

Correction of Background Trend in ROIs

The density of neighboring and overlapping breast tissue may affect the background gray levels of ROIs. In general, background tissue does not directly relate to the presence of a mass, but it may affect the segmentation and feature extraction results used in computerized analysis. To reduce the influence of background tissue to masses, we applied an algorithm that could correct the gray-level distribution and make masses salient in the ROIs. The method was chosen on the basis of the topographic form of the ROIs. The topographic form of masses is higher than that of background tissue. Masses typically contain high-frequency information, whereas background tissue contains low-frequency information. Because of this, plane fitting based on the least-squares method (26) was applied. Figure 3 shows one spiculated mass (Fig 3a) and one circumscribed mass (Fig 3b) depicted on two ROIs. Figure 3c,d illustrate the fitting plane image of the original ROIs, and Figure 3e,f show the corresponding ROIs obtained by subtraction of the plane image from the original ROIs. The processing substantially reduces the variation of the background gray levels, resulting in a "flat background" in the ROI while retaining high-frequency information (ie, masses). Next, to improve mass contrast, the gamma correction procedure and a simple Gaussian filter were used sequentially. This image-processing procedure generated the background-trend-corrected ROIs (Fig 3g,h). From these ROIs, one can observe that the influence of the background structures is reduced, and masses become salient objects.

Segmentation of Mass Region

After background trend correction, our computerized method applies three steps to segment mass region and

detect boundary spiculation level, as described in the following.

Step 1: Initial segmentation using the principle of maximum entropy

In this step, a mass region is segmented with the initial detection of a mass shape within an ROI using the principle of maximum entropy. Entropy is a basic concept in information theory proposed by Shannon (27). For a discrete variable Y with a set of values y_1, y_2, \dots, y_N , Equation 1 is defined as entropy on the basis of the probability distribution of Y . In general, higher entropy means more information contained in a system.

$$H(Y) = - \sum_{i=1}^N P(Y = y_i) \log P(Y = y_i). \quad (1)$$

The principle of maximum entropy is one of the most important threshold selection methods in image processing. It was first proposed by Pun (28) and aims to divide histograms of images into independent classes, with the sum of entropies for all classes defined as the maximum. The problem can be formalized as follows. For a set P , P is divided into k subsets without overlap, $P = P_1 \cup P_2 \cup \dots \cup P_k$. The sum of subset entropies is represented as

$$H(P) = H(P_1) + H(P_2) + \dots + H(P_k). \quad (2)$$

Next, optimal thresholds are selected to divide the histogram of P to achieve the maximum $H(P)$ value. The purpose of this step is to partition pixels of ROI into mass and background tissue. It means that an adaptive threshold should be found to classify the pixels into two classes, A and B. The parameter k in Equation 2 equals 2, and p_0, p_1, \dots, p_n is defined as the probability distribution of the gray levels of background-trend-corrected ROIs. If s is set to be the threshold, two probability distributions can be obtained. One is the probability distribution of $1 \sim s$ gray levels, and the other is the probability distribution of $s + 1 \sim n$ gray levels. The two probability distributions are

$$A: \frac{p_0}{P_T}, \frac{p_1}{P_T}, \dots, \frac{p_s}{P_T}; B: \frac{p_{s+1}}{1 - P_T}, \frac{p_{s+2}}{1 - P_T}, \dots, \frac{p_n}{1 - P_T},$$

where $P_T = \sum_{i=0}^s p_i$. (3)

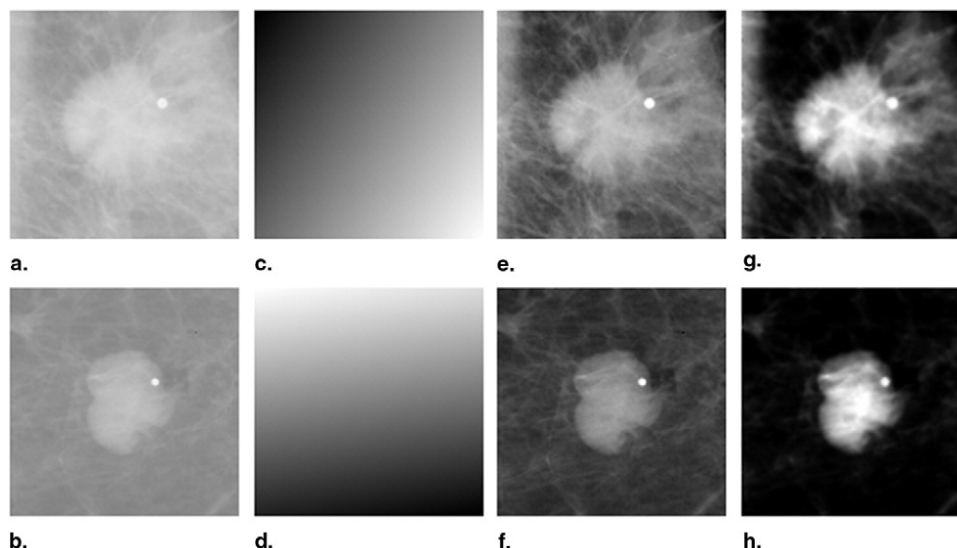


Figure 3. The original regions of interest (ROIs), the fitting planes, the subtracted ROIs, and the background-trend-corrected ROIs for a spiculated mass (a) and a circumscribed mass (b). (c,d) Fitting plane image of the original ROIs on the basis of the least-squares method. (e,f) Subtraction of the plane image from the original ROIs. (g,h) Background-trend-corrected ROIs.

The respective entropies for A and B are

$$H(A) = - \sum_{i=0}^s \frac{P_i}{P_T} \log \frac{P_i}{P_T}; \text{ and} \quad (4)$$

$$H(B) = - \sum_{i=1+s}^n \frac{P_i}{1 - P_T} \log \frac{P_i}{1 - P_T}.$$

$$s = \arg\{\max_s [H(A) + H(B)]\}. \quad (5)$$

The optimal threshold s should satisfy Equation 5. With this threshold, the maximum entropy (or maximum information) that represents the optimal division of the image would be obtained.

Figure 4a,b shows the segmentation results of the background-trend-corrected ROIs (as shown in Fig 3) on the basis of the principle of maximum entropy. The images are illustrated in binary form; a value of 255 (white) indicates an object (mass) pixel, and a value of 0 (black) indicates a background pixel. To obtain the initial contour of the mass region, a morphologic dilation operation with a 3×3 square mask is applied to the binary image. Figure 4c,d shows the results of the initial boundary contour after subtraction of the original segmented image from the dilated image. Because of the method depicted in ROI extraction, the center of the ROI is the brightest pixel (with the minimum digital value) inside the seg-

mented mass region. Hence, we treat the first connected area boundary on the direction pointing outward from the center as the final segmented outline of this stage, as shown in Figure 4e,f. In addition, Figure 4g,h shows the segmentation results highlighted on the original ROIs.

Step 2: Segmentation refinement with active-contour model

We then applied an active-contour (or snake) model (29) to improve mass boundary segmentation. An active-contour model is an energy minimization method that has been widely used in applications of computer vision and pattern recognition, including edge detection, shape segmentation, and motion tracking. However, active contour depends heavily on local edge-based image features to guide its convergence. This makes active-contour models sensitive to noise and the initial estimation. Hence, good initialization is often required. Because the preliminary results showed that initial mass segmentation results obtained in the first step of the method generated reasonable mass shapes for most masses, we used it as the initial contour (starting point) in the active-contour model.

A snake is a curve defined within an image domain that can move under the influence of internal forces within the curve itself and external forces derived from the image data. The actions of a snake are directed by an energy function. A snake is defined as $v(s) = [x(s), y(s)]$,

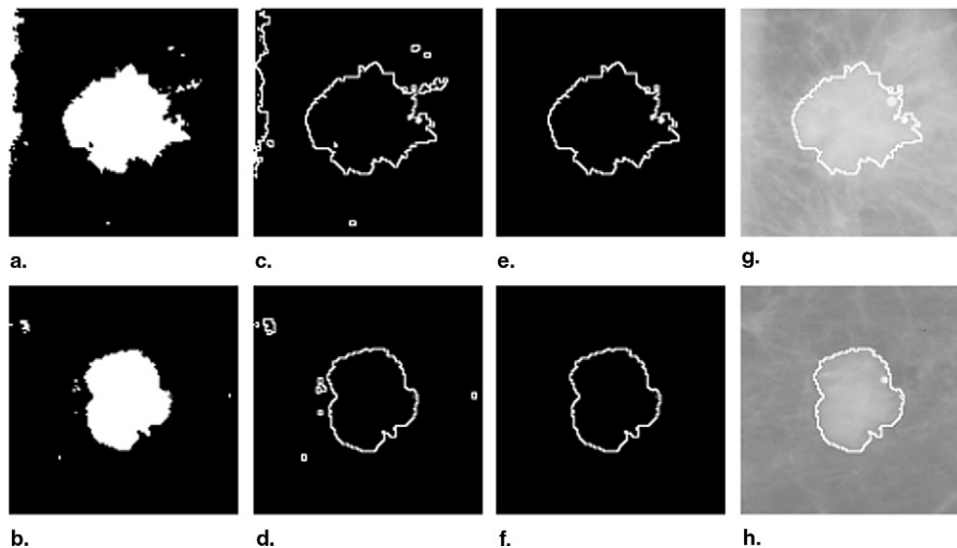


Figure 4. Initial segmentation procedures applied to two masses shown in Figure 3, including the threshold result based on the principle of maximum entropy (a, b), dilation result (c, d), the first connected area boundary (e, f), and the boundary contour overlaid on the original region of interest (g, h).

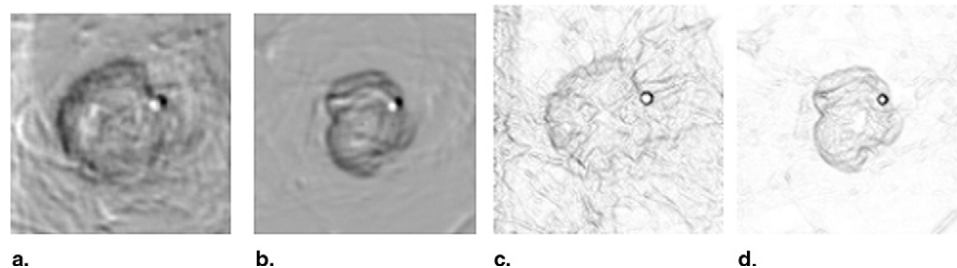


Figure 5. The gradient of a background-trend-corrected region of interest (ROI) obtained with our method (a,b) and the gradient of a background-trend-corrected ROI obtained with the general method (c,d).

where $x(s)$ and $y(s)$ are x and y coordinates along the contour, and $s \in [0,1]$. The general description of the energy function is given in Equation 6. It consists of internal energy and external energy:

$$E_{\text{snake}} = \int_0^1 E_{\text{int}}[v(s)]ds + E_{\text{ext}}[v(s)]ds. \quad (6)$$

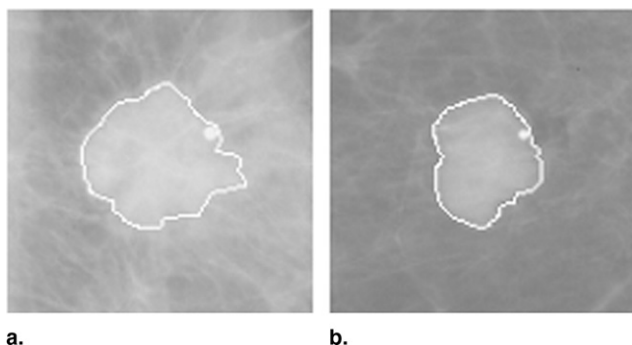
The internal energy is usually written as $E_{\text{int}} = [\alpha(s)|v_s(s)|^2 + \beta(s)|v_{ss}(s)|^2]/2$. It is composed of a first-order term controlled by $\alpha(s)$ and a second-order term controlled by $\beta(s)$. The first-order term $v_s(s)$ is treated as elastic energy, which causes the snake to shrink like an elastic rubber band. The second-order term $v_{ss}(s)$ makes the snake behave like a thin metal strip and is responsible for the smoothness of the contour. The external energy is derived from the image data. It attracts the snake to salient image contours, such as edges, lines, and subjective contours. For this purpose, external energy can be defined

as intensity or gradient of the image. In 1998, Xu and Prince (30) proposed gradient vector flow to deal with the two key difficulties of the traditional active-contour model. The gradient vector flow field, the vector $V(x, y) = [u(x, y), v(x, y)]$, minimizes the energy function

$$\varepsilon = \int \int \mu(u_x^2 + u_y^2 + v_x^2 + v_y^2) + |\nabla f|^2 |V - \nabla f|^2 dx dy, \quad (7)$$

where $|\nabla f|$ is the gradient of the original image. The gradient of the original image is identified as an edge map in which each pixel is assigned a value according to the edge strength. Mostly, pixels with large values represent object boundaries. The calculated edge magnitudes and capture range of the edge map directly affect the gradient vector flow field.

In this study, we applied our previously proposed method (31) to compute the edge map. Figure 5a,b shows



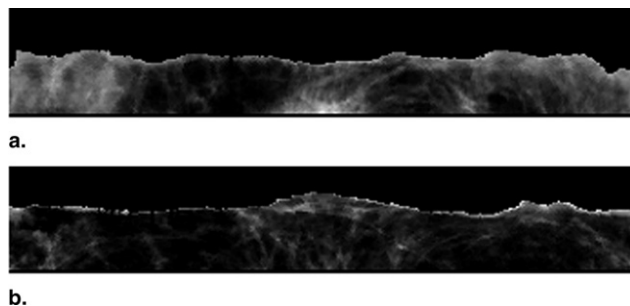
a.
Figure 6. The refined boundary contours overlaid on the original region of interest in Figure 3a (a) and 3b (b), respectively.

the gradient of a background-trend-corrected ROI obtained with our method, and Figure 5c,d shows the gradient of a background-trend-corrected ROI obtained with the general method (30). From Figure 5, it can be seen that the gradient computed using our method is more obvious than that computed using the general method, and it results in increasing the capture range of the external force field. To apply the active-contour (snake) algorithm to segment the boundaries of the suspected mass regions, we downloaded and tested an available active-contour program (GVF Snake Demo version 1.0 beta [32]). We then modified this program with the proposed gradient image and integrated it into our method. Figure 6a,b shows the refined results of the original ROI shown in Figure 3a,b after applying the active-contour model to the images.

Step 3: Detection of spiculation level

In this step, a line or edge detection filter is applied to detect linear structures surrounding the mass boundary contour detected in previous steps. Although not all of the linear structures are related to the mass boundary spiculation, we define the spiculated lines as those that must be located approximately in directions radiating from the center of the mass region, whereas most blood vessel or other tissue lines do not have such an orientation characteristic. Hence, one useful feature of detecting spiculated lines is their orientation, and we designed a special line detector to detect mass boundary spiculation.

The detection of spiculations with the line detector is complicated by the fact that the search direction for the spiculation changes with the shape of mass and the curvature of its margin. To overcome this problem, we first transformed original coordinates (x, y) of the background-trend-corrected ROI containing the mass boundary segmented by the active-contour model into polar coordinates



a.
b.
Figure 7. The polar coordinate representation image of the background-trend-corrected region of interest shown in Figure 3g (a) and 3h (b) processed with the refined result by the active-contour model, respectively.

(θ, d) . The center of the background-trend-corrected ROI defines the origin for the coordinate transform. The x axis in the polar coordinate image represents the angle θ from 0 to 2π , whereas the y axis represents the radius d from 0 to half of the ROI size (64 pixels). The transformed images are illustrated in Figure 7. In the polar coordinate representation image, pixel value 0 represents the pixels inside the segmented result obtained with the snake. After the transformation, pixels along a radial line from the center to the border of the background-trend-corrected ROI are mapped to a column of the polar coordinate image. Pixels at a constant distance radiating from the center of the background-trend-corrected ROI are mapped to a row of the polar coordinate image. In this way, the border of a mass is expected to appear approximately as a horizontal edge, and spiculations are expected to appear approximately as vertical lines in the polar system.

On the basis of the orientation characteristic of spiculations, we defined a line detector that could detect vertical line structures on the polar coordinate image. The line detector contains a series of edge filter templates, which are shown in Figure 8. They are used to obtain vertical or nearly vertical gradient transformation. Each edge filter template is applied to convolve the polar coordinate image respectively. With these defined templates, five values at each pixel are obtained, and the largest among the absolute of these five values is denoted as the last gray value for the pixel. If the largest value is greater than 255, the pixel value is denoted as 255. The obtained gradient transformation images are represented in Figure 9. Next, the threshold method with an optimal threshold value of 255 is used to convert the filtered image into a binary image. All pixels with digital values smaller than 255 are assigned values of 0, whereas other pixels with digital values are 255 are converted to 1. The binary im-

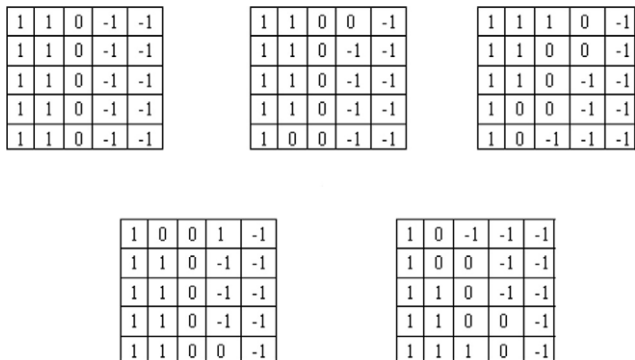


Figure 8. A series of edge filter templates.

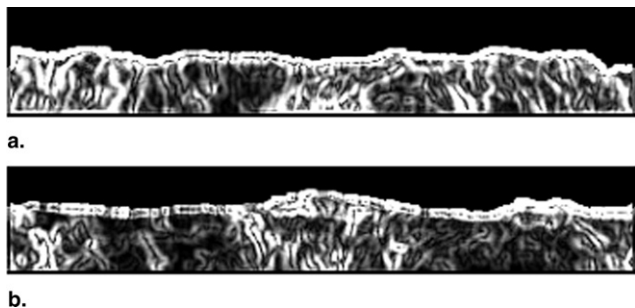


Figure 9. The gradient transformation image of Figure 7a (a) and 7b (b), respectively.

age is transformed into original coordinates (x, y), and all detected lines with the mass boundary that we had already segmented are combined. Then a labeling method is applied to extract the first connected area boundary on the direction pointing outward from the center. The extracted connected area boundary is treated as the final segmented result of this segmentation algorithm. The results are shown in Figure 10.

Evaluation of the Performance of the Method

Although spiculation level is an important feature in detecting and classifying breast masses, a previous study has indicated large interobserver variation in subjectively rating mass boundary spiculation levels (33). Hence, mass boundary spiculation is a very subjective concept, and there is no “ground truth” to evaluate the severity of spiculation levels and the accuracy of computerized methods. To “quantitatively” evaluate the accuracy of our spiculation detection method, we applied a computed measure index to assess the spiculation levels of different mass regions. This quantitative measure is defined as $SI = P^2/A$, where P represents the detected number of perimeter pixels, and A is the mass area (the total pixels de-

tected inside the mass region). Higher spiculated mass has more pixels detected in the perimeter, which generates a larger SI value. This feature has been widely accepted as an effective evaluation index for spiculation in CAD methods for mammography (12,34).

After applying our automated computer method to the image data set to detect mass boundary spiculation and compute total 211 SI values (including 106 for circumscribed masses and 105 for spiculated masses), we applied ROC analysis (35) to evaluate the abilities of the spiculation measure in classification between these circumscribed and spiculated masses. Specifically, we used a publicly available ROC program (ROCFIT [36]) that uses a maximum likelihood statistical method to fit the experimental data, generate a smoothed ROC curve, and compute the area under the ROC curve (A_z), that is used as a performance index in our method.

RESULTS

The difference of two histogram distributions of SI values between 106 circumscribed mass regions and 105 spiculated mass regions was compared and plotted (Figure 11). On average, the computed SI values of spiculated mass regions were higher than those of circumscribed mass regions. In this data set, the average SI value for the 106 circumscribed mass regions was 4.4 ± 3.1 , and the average SI value for the 105 spiculated mass regions was 7.1 ± 4.8 . For example, the computed SI values for the two mass regions as shown in Figure 3a,b were 7.0 and 3.0, respectively. When a threshold ($SI = 5.0$) was applied to classify between spiculated and circumscribed mass regions, 140 of 211 (66.4%) of mass regions, including 57 spiculated mass regions (54.3%) and 83 circumscribed mass regions (78.3%) were classified into the correct group (category), whereas the remaining 71 (33.6%) regions, including 48 spiculated mass regions (45.7%) and 23 circumscribed mass regions (21.7%), were misclassified in the data set used in this study. Thus, the overall accuracy at this threshold level is 66.4%, with 54.3% sensitivity and 78.3% specificity. The corresponding false-negative rate is 0.23 (48 of 211) and false-positive rate is 0.11 (23 of 211). On the basis of the two histogram distributions shown in Figure 11, a computed ROC curve is plotted in Figure 12. It shows the overall performance of this new computerized method to detect and distinguish between spiculated and circumscribed mass

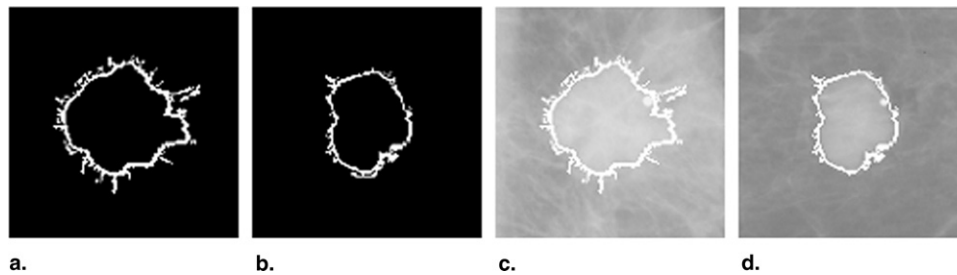


Figure 10. The final segmented results of this segmentation algorithm in binary form (a,b) and the final segmented results shown on the original regions of interest (c,d).

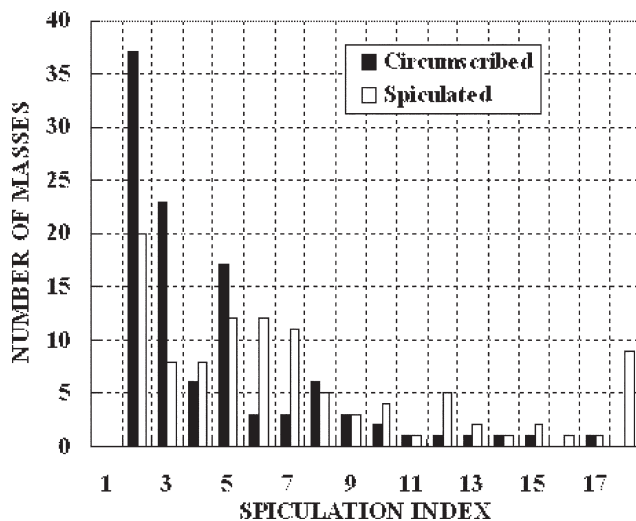


Figure 11. The histogram distribution of two types of mass regions using the spiculation index.

regions in the data set selected for this study. The computed area under the ROC curve (A_2) was 0.701 ± 0.027 .

DISCUSSION

Mass boundary spiculation is a well-recognized image feature in both visual and automated detection between true-positive and false-positive masses as well as classification between malignant and benign masses (18). It is also a very important and sensitive feature for improving visual similarity of similar reference masses selected by interactive CAD methods (23). As a result, the automated detection of spiculated mass regions has attracted substantial research interest in CAD development. Although previous studies have suggested that using CAD methods involving automatically detected mass spiculation-related features could achieve higher performance (in particular for the classification of malignant and benign masses)

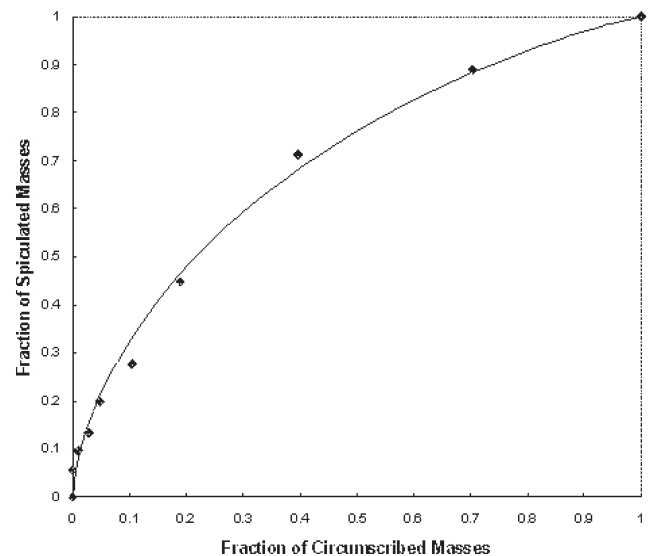


Figure 12. Receiver-operating characteristic curve for distinguishing between spiculated and circumscribed mass regions.

(19–22), the performance of these computer methods in actually detecting mass spiculation levels or classifying between spiculated and nonspiculated (eg, circumscribed) mass regions has not been quantitatively assessed and reported in detail. Without knowing the actual performance (including accuracy and robustness) of the methods in detecting mass spiculation levels, it is difficult to assess the exact or the maximum potential contribution of the computed mass spiculation-related features to the overall improvement of CAD performance. In this preliminary study, we focused on developing a new automated approach to detect mass boundary spiculation levels and assessing the method's performance in detecting and distinguishing between spiculated and circumscribed masses using a relatively large image data set and ROC analysis.

To automatically detect the spiculated lines (or curves) connected to the mass boundary, the accurate segmentation of mass boundary contour is an important procedure

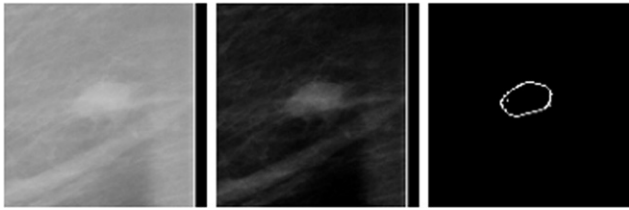


Figure 13. An example of the misclassification of a spiculated mass region.

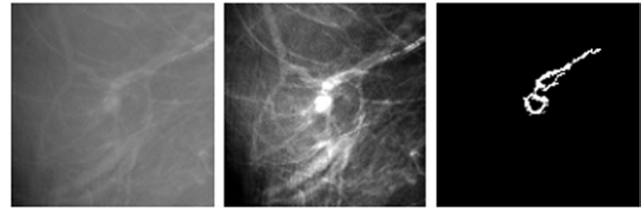


Figure 14. An example of the misclassification of a circumscribed mass region.

that determines the success or failure of a method in correctly detecting and classifying between spiculated and circumscribed mass regions. In our method, we implemented a unique algorithm to segment mass boundaries. The segmentation algorithm combined the principle of maximum entropy with an active-contour model. The results demonstrated that this algorithm could effectively segment the boundaries of most typical masses in the data set used in this study. This algorithm tends to smooth mass region boundaries, and the segmented mass boundary contour closely matches the real mass boundary, except that it misses the attached spiculated lines (as shown in Fig 6). Then, the method applies a specially designed line detector to identify the connected spiculated lines. The detector includes several image processing steps: (1) coordinate transformation from original (x, y) to polar coordinates (θ, d) , (2) filtering transformed images with a series of edge filter templates, and (3) line detection and labeling. The results indicated that this algorithm could detect a high fraction of spiculated lines, even in very low resolution images (with approximately $400 \times 400 \mu\text{m}$ pixel size). As a result, this new computer method can efficiently detect and correctly classify the majority of typical spiculated and circumscribed mass regions. For example, when a threshold ($SI = 5.0$) was applied to distinguish between spiculated and circumscribed mass regions, approximately two thirds (140 of 211) of mass regions were classified into the correct group.

We recognize that the classification rate or ROC-based performance of our method in distinguishing between spiculated and circumscribed mass regions remains relatively lower (with an A_z value of 0.701 ± 0.027 , as shown in Figure 12). There are two reasons for this low A_z value when applying our computer method. First, the method fails to detect a fraction of spiculated lines for some low-conspicuity mass regions surrounded with dense fibroglandular breast tissue. Second, the method misrecognizes other surrounding linear structure (eg, blood vessels) as spiculated lines connected to the circumscribed mass regions. Figure 13

demonstrates an example in which the method classified a spiculated mass region as a circumscribed mass region ($SI = 2.0$), and Figure 14 shows another example in which a circumscribed mass region was classified as a spiculated region ($SI = 14.0$). Therefore, achieving highly accurate and robust results with current computerized methods in detecting mass boundary spiculation remains a major technical challenge (particularly for CAD methods that detect breast masses using images with low spatial resolution).

Despite the limitations of our method's performance and the large interobserver variability in rating mass spiculation levels (12,33), which may affect the reliability of the "truth" file, the overall performance reported in this study (Figure 12) provides a useful reference of method performance in automatically detecting mass boundary spiculation levels. This performance reference level is not only useful for our future studies that aim to improve the performance and robustness of our computerized method in detecting and classifying spiculated masses, it can also be easily used by other research groups to compare and demonstrate the performance improvement of their computer methods, because this performance reference was generated using a publicly available image data set (the DDSM).

In summary, we developed a new computerized method with a number of unique characteristics to detect spiculated mass regions and applied a simple SI to quantify mass spiculation levels. We assessed and reported the overall performance level of the method using a data set that included 105 spiculated and 106 circumscribed mass regions selected from a publicly available image database. The results of this preliminary study demonstrate that the overall performance of the computerized method in detecting mass spiculation levels was relatively low because of the remaining technical challenge in the automated detection of mass spiculation levels. Although similar performance evaluations have not been performed and reported in previous studies by other research groups, we

believe that this performance level is not a limitation that applies only to our present computerized method. Therefore, further development and evaluation studies are needed in this area to improve the performance and robustness of computerized methods in detecting and quantifying mass boundary spiculation levels.

REFERENCES

- Rennie J, Rusting R. Making headway against cancer. *Sci Am* 1996; 275:56–59.
- Mettlin C. Global breast cancer mortality statistics. *CA Cancer J Clin* 1999; 49:135–137.
- Miller AB. Mammography: reviewing the evidence. *Epidemiology aspects*. *Can Fam Physician* 1993; 39:85–90.
- Smith RA. Breast cancer screening among women younger than age 50: a current assessment of the issues. *CA Cancer J Clin* 2000; 50: 312–336.
- Tabar L, Vitak B, Chen HH, et al. Beyond randomized controlled trials: organized mammographic screening substantially reduces breast carcinoma mortality. *Cancer* 2001; 91:1724–1731.
- Nishikawa RM. Current status and future directions of computer-aided diagnosis in mammography. *Comput Med Imaging Graph* 2007; 31: 224–235.
- Brem RF, Hoffmeister JW, Zisman G, et al. A computer-aided detection system for the evaluation of breast cancer by mammographic appearance and lesion size. *AJR Am J Roentgenol* 2005; 184:893–896.
- Gur D, Stalder JS, Hardesty LA, et al. Computer-aided detection performance in mammographic examination of masses: assessment. *Radiology* 2004; 223:418–423.
- Freer TM, Ullissey MJ. Screening mammography with computer-aided detection: prospective study of 12,860 patients in a community breast center. *Radiology* 2001; 220:781–786.
- Khoo LA, Taylor P, Given-Wilson RM. Computer-aided detection in the United Kingdom National Breast Screening Programme: prospective study. *Radiology* 2005; 237:444–449.
- Sahiner B, Petrick N, Chan H, et al. Computer-aided characterization of mammographic masses: accuracy of mass segmentation and its effects on characterization. *IEEE Trans Med Imaging* 2001; 20: 1275–1284.
- Zheng B, Mello-Thoms C, Wang XH, et al. Interactive computer aided diagnosis of breast masses: computerized selection of visually similar image sets from a reference library. *Acad Radiol* 2007; 14:917–927.
- Petrick N, Chan HP, Wei D, et al. Automated detection of breast masses on mammograms using adaptive contrast enhancement and texture classification. *Med Phys* 1996; 23:1685–1696.
- Zheng B, Chang YH, Gur D. Computer detection of masses in digitized mammograms using single-image segmentation and a multilayer topographic feature analysis. *Acad Radiol* 1995; 2:959–966.
- Catarious DM, Baydush AH, Floyd CE. Incorporation of an iterative, linear segmentation routine into a mammographic mass CAD system. *Med Phys* 2004; 31:1512–1520.
- Timp S, Karssemeijer N. A new 2D segmentation method based on dynamic programming applied to computer aided detection in mammography. *Med Phys* 2004; 31:958–971.
- Te Brake GM, Karssemeijer N. Segmentation of suspicious densities in digital mammograms. *Med Phys* 2001; 28:259–266.
- Vyborny CJ, Doi T, O'Shaughnessy KF, et al. Breast cancer: importance of spiculation in computer-aided detection. *Radiology* 2000; 215: 703–707.
- Kegelmeyer WP, Pruneda JM, Bourland PD, et al. Computer-aided mammographic screening for spiculated lesions. *Radiology* 1994; 191: 331–337.
- Karssemeijer N, Te Brake GM. Detection of stellate distortions in mammograms. *IEEE Trans Med Imaging* 1996; 15:611–619.
- Huo Z, Giger ML, Vyborny CJ. Analysis of spiculation in the computerized classification of mammographic masses. *Med Phys* 1995; 22:1569–1579.
- Sahiner B, Chan HP, Petrick N, et al. Improvement of mammographic mass characterization using spiculation measures and morphological features. *Med Phys* 2001; 28:1455–1465.
- Zheng B, Lu A, Hardesty LA, et al. A method to improve visual similarity of breast masses for an interactive computer-aided diagnosis environment. *Med Phys* 2006; 33:111–117.
- Heath M, Bowyer K, Kopans D, et al. The Digital Database for Screening Mammography. Presented at: 5th International Workshop on Digital Mammography; June 2000; Toronto, Canada.
- Eltoumy NH, Tourassi GD, Elmaghraby AS. A concentric morphology model for the detection of masses in mammography. *IEEE Trans Med Imaging* 2007; 26:880–889.
- Yuan Y, Giger ML, Li H, et al. A dual-stage method for lesion segmentation on digital mammograms. *Med Phys* 2007; 34:4180–4193.
- Shannon CE. A mathematical theory of communication. *Bell Syst Tech J* 1948; 27:379–423, 623–656.
- Pun T. A new method for gray level picture thresholding using the entropy of the histogram. *Signal Process* 1980; 2:233–237.
- Kass M, Witkin A, Terzopoulos D. Snake: active contour models. *Int J Comput Vision* 1987; 1:321–331.
- Xu C, Prince JL. Snakes, shapes, and gradient vector flow. *IEEE Trans Image Processing* 1998; 7:359–369.
- Song E, Jiang L, Meng B, et al. Mass edge detection in mammography based on plane fitting and dynamic programming. Presented at: 2007 ACM Symposium on Applied Computing; March 11–15, 2007; Seoul, Korea.
- GVF snake demo. Available at: <http://iacl.ece.jhu.edu/projects/gvf/snakedemo/>. Accessed September 2, 2006.
- Zheng B, Abrams G, Leader JK, et al. Mass margins spiculations: agreement between ratings by observers and a computer scheme. *Proc SPIE* 2007; 6514:65141P.
- Li L, Zheng Y, Zhang L, et al. False-positive reduction in CAD mass detection using a competitive classification strategy. *Med Phys* 2001; 28:250–258.
- Metz CE, Wang PL, Kronman HB. Maximum-likelihood estimation of receiver operating characteristic (ROC) curves from continuously-distributed data. *Stat Med* 1998; 17:1033–1053.
- Metz CE. ROCFIT 0.9B beta version. Available at: <http://www.radiology.uchicago.edu/krl/>. Accessed December 3, 2005.